





Time-dependent physics of single-surface multipactor discharge with two carrier frequenciesAsif Iqbal ¹, Patrick Y. Wong ¹, De-Qi Wen ^{1,2}, Shu Lin,^{2,3} John Verboncoeur,^{1,2} and Peng Zhang ^{1,*}¹*Department of Electrical and Computer Engineering, Michigan State University, East Lansing, Michigan 48824-1226, USA*²*Department of Computational Mathematics, Science and Engineering, Michigan State University, East Lansing, Michigan 48824, USA*³*Key Laboratory for Physical Electronics and Devices of the Ministry of Education, Xi'an Jiaotong University, Xi'an 710049, China*

(Received 12 June 2020; revised 18 August 2020; accepted 11 September 2020; published 2 October 2020)

This work investigates the time-dependent physics of multipactor discharge on a single dielectric surface with a transverse rf electric field of two carrier frequencies using a multiparticle Monte Carlo simulation model with adaptive time steps. The effects of the relative strength and phase, and the frequency separation between the two carriers are studied. Closed Lissajous curves are obtained to describe the relationship between the rf electric field parallel to the surface and the normal surface charging field in the ac saturation state. It is found that two-frequency operation can reduce the multipactor strength compared to single-frequency operation with the same total rf power, though the effect of the frequency separation is not prominent on multipactor susceptibility. Formation of beat waves is observed in the temporal profiles of the normal electric field due to surface charging with a noninteger frequency ratio between the two carrier modes. Phase space evolution of multipactor electrons is examined, revealing a periodic bunching and debunching of electrons in the surface normal direction, but a gradual debunching effect in the direction tangential to the dielectric surface. Migration of the multipactor trajectory is also demonstrated for different configurations of the two-frequency rf fields.

DOI: [10.1103/PhysRevE.102.043201](https://doi.org/10.1103/PhysRevE.102.043201)**I. INTRODUCTION**

Multipactor [1–7] is an ac discharge in which a high frequency rf field creates an electron avalanche sustained through secondary electron emission from a metallic or dielectric surface. It may cause breakdown of dielectric windows [8–11], erosion of metallic structures, melting of internal components, and perforation of vacuum walls [2] that adversely affect various applications, including high power microwave (HPM) sources, rf accelerators [10], and space-based communication systems [12,13]. Multipactor induced degradation of signal quality in space-based communications has also become a major issue [14]. Multipactor discharge may also cause rf noises [15], intermodulation distortion [16], and higher harmonic generation [16,17].

There has been continued interest in multipactor under multicarrier operation [18–21] since many modern communication systems employ multicarrier rf transmission [22,23]. A primary requirement for modern satellites and spacecraft is the ability to perform complex multifrequency communication through a restricted frequency spectrum [14]. Additionally, in recent times, due to restricted availability of orbital slots, several advanced communication missions are being frequently incorporated in a single satellite payload rendering multifrequency communication essential [24]. When a number of carrier waves are transmitted simultaneously at different frequencies through the system, modulation of the signal amplitude takes place which may significantly modify the conditions for multipactor breakdown [23]. Semenov *et al.*

[22] previously showed that with two-frequency rf operation, suppression of multipactor breakdown can be achieved in a metallic gap when the two carrier waves have close but separated frequencies. By employing the two-frequency rf field, Rice and Verboncoeur [25] demonstrated the migration of multipactor trajectories to specific desirable locations in the parallel plate geometry for the purpose of cleaning the structure or to reduce further multipactor susceptibility. Multipactor under multicarrier operations has also been studied in two-surface [14,22,25,26], and microstrip [27] geometries.

For the single-surface geometry, Wen *et al.* [28] demonstrated suppression of multipactor discharge due to nonsinusoidal rf wave shapes, which is intrinsically a multifrequency waveform, using particle-in-cell (PIC) [29,30] and multiparticle Monte Carlo (MC) [16,31] simulations. Iqbal *et al.* employed single-particle MC simulation to study the single-surface multipactor susceptibility [3,23] for two carrier frequencies. A multiparticle MC method was also developed to investigate two-frequency single-surface multipactor discharge in the temporal [31] and the frequency [16] domain. However, there is still a lack of a comprehensive study of the time-dependent physics of a two-frequency multipactor on a dielectric, and the parametric dependence of the multipactor dynamics is largely unknown.

In this paper, we examine in detail the time-dependent physics of multipactor discharge on single dielectric surfaces with an rf signal consisting of two carrier frequencies, using a multiparticle MC simulation model [31]. The description of the model is presented in Sec. II. Section III presents the temporal profiles of the secondary electron yield, and the electric field normal to the surface that corresponds to the multipactor strength in the system, at various combinations of

*pz@egr.msu.edu

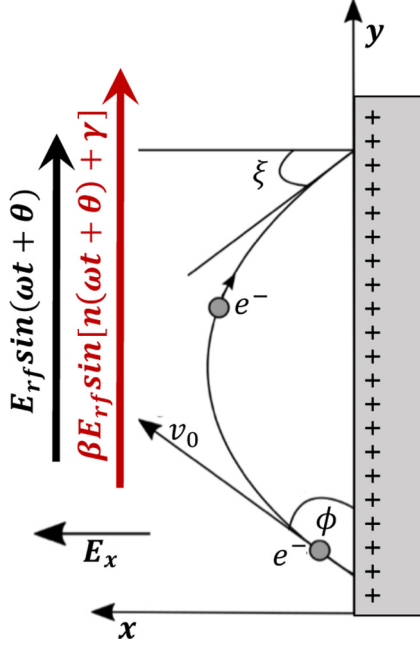


FIG. 1. Schematic of the single-surface multipactor discharge in a normal electric field and a parallel rf field with two carrier frequencies.

the frequency separation, relative strength, and relative phase between the two carrier frequencies of the rf electric field. We obtain the multipactor susceptibility diagrams from our temporal studies in Sec. IV. In Sec. V, the multipactor electron trajectories and their corresponding distributions in phase space of velocity and position are analyzed. In Sec. VI we study the effect of frequency separation between the two carrier modes on the susceptibility boundaries and the time-dependent physics. Concluding remarks are given in Sec. VII.

II. ELECTRON DYNAMICS AND MULTIPARTICLE MONTE CARLO MODEL

Figure 1 shows a schematic of single-surface multipactor discharge. An rf electric field $E_y = E_{\text{rf}} \sin(\omega t + \theta) + \beta E_{\text{rf}} \sin[n(\omega t + \theta) + \gamma]$ is applied parallel to the surface along the y direction. Here E_{rf} is the peak electric field strength; ω is the angular frequency; and θ is the initial phase of the electric field, of the fundamental carrier mode. β is the field strength of the second carrier mode relative to the fundamental mode, γ is the relative phase of the second carrier mode when $(\omega t + \theta) = 0$ or an integer multiple of 2π , and n is the ratio of the two carrier frequencies. The multipactor electrons are subjected to forces imposed by this parallel rf electric field and the normal electric field E_x originating from the residual charge on the dielectric acting along the x direction (Fig. 1). Referring to Fig. 1, the flight trajectory of a multipactor electron is governed by the force law,

$$m \frac{\partial \vec{v}}{\partial t} = -|e| \{ \vec{E}_{\text{rf}} \sin(\omega t + \theta) + \beta \vec{E}_{\text{rf}} \sin[n(\omega t + \theta) + \gamma] + \vec{E}_x \}. \quad (1)$$

The velocity of the electron is obtained as

$$v_x = -\frac{|e|}{m} E_x t + v_0 \sin \phi, \quad (2a)$$

$$v_y = \frac{|e|}{m\omega} E_{\text{rf}} \left(\cos(\omega t + \theta) - \cos \theta + \frac{\beta}{n} \{ \cos[n(\omega t + \theta) + \gamma] - \cos(n\theta + \gamma) \} \right) + v_0 \cos \phi, \quad (2b)$$

where v_0 and ϕ are the emission speed and emission angle with respect to the surface of the multipactor electron, respectively. From Eq. (2), we obtain the instantaneous position of a multipactor electron as

$$x = -\frac{|e|}{2m} E_x t^2 + v_0 t \sin \phi + x_0, \quad (3a)$$

$$y = \frac{|e|}{m\omega} E_{\text{rf}} \left[\frac{1}{\omega} [\sin(\omega t + \theta) - \sin \theta] - t \cos \theta + \frac{\beta}{n} \left(\frac{1}{n\omega} \{ \sin[n(\omega t + \theta) + \gamma] - \sin(n\theta + \gamma) \} - t \cos(n\theta + \gamma) \right) \right] + v_0 t \cos \phi + y_0. \quad (3b)$$

Here x_0 and y_0 account for initial position of the particles at $t = 0$. The transit time τ of an electron in flight is calculated by solving Eq. (3a) for $x = 0$. Note that in our multiparticle Monte Carlo simulation, the solutions to Eq. (1) given in Eqs. (2a) and (2b), and (3a) and (3b), apply only during the intervals between any two consecutive impacts from the entire ensemble of particles upon the surface, during which the normal electric field E_x remains constant (see Fig. 2 of Ref. [16] and Fig. 1 of Ref. [31] for details). E_x is updated only upon the impact of any particle onto the dielectric surface. The possible space-charge effects due to multipactor electrons [30–34] are not considered beyond the varying strength of E_x [31].

The average number of secondary electrons produced by the impact of each primary electron upon the surface, i.e., the secondary electron yield, δ , is a function of the impact energy of the primary electron, E_i , and the angle to the normal, ξ , at which it strikes the surface [35–38]. It also depends on material properties translating into two parameters, the maximum yield, δ_{max} , and the energy at which it occurs, E_{max} . We adopt Vaughan's empirical formula [35,36] in our simulation, as discussed in Ref. [23], to estimate the secondary electron yield δ .

To investigate the time-dependent physics of the multipactor discharge, we follow the algorithm described in detail in Refs. [16,31]. A brief description is included here for completeness. We start the simulation with N weighted macroparticles emitted at time $t = 0$ from the initial position $x = 0$ and $y = 0$ of a surface. An initial electric field E_{x0} ($E_{x0} \sim E_{\text{rf}}/30$) is assigned normal to the surface and the initial surface charge is calculated as $N_s = 2AE_{x0}\epsilon_0/|e|$, where A is the area of the dielectric surface (1 m^2) and ϵ_0 is the free space permittivity. The same amount of negative charge is evenly distributed to the N initial macroparticles. We follow the trajectory of these macroparticles over a large number of impacts in a MC simulation [16,31]. Each time a

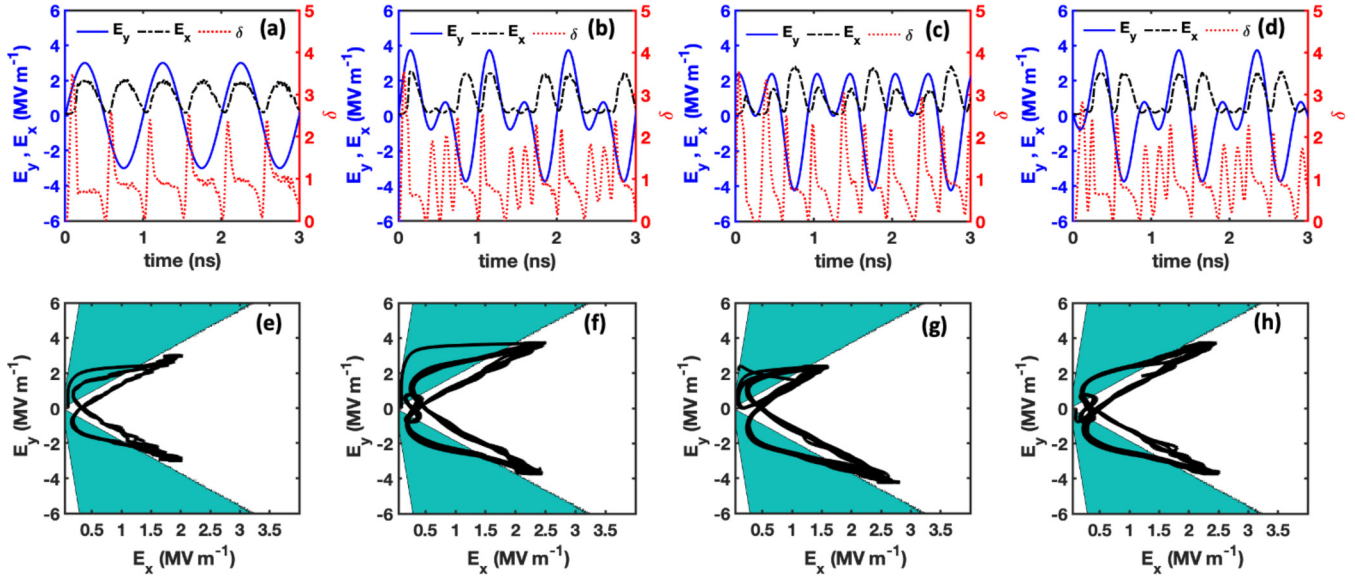


FIG. 2. Top row: Instantaneous rf electric field E_y (solid blue lines), normal electric field E_x (broken black lines), and secondary electron yield δ (dotted red lines), for (a) single-frequency rf field, $\beta = 0$; (b) two carrier frequencies of the rf field with frequency ratio $n = 2$, relative strength of the second carrier frequency, $\beta = 1$, and initial relative phase of the second carrier frequency, $\gamma = 0$; (c) two carrier modes with $n = 2$, $\beta = 1$, $\gamma = \pi/2$; and (d) two carrier modes with $n = 2$, $\beta = 1$, $\gamma = \pi$. Bottom row: (e–h) The corresponding plots of trajectories of the electric field $[E_x(t), E_y(t)]$ for (a–d), respectively. The shaded cyan region is the multipactor susceptibility region obtained by applying constant electric field, $E_{y,dc}$, parallel to the surface [29,31,39]. In (a)–(d), the average secondary electron yield $\delta_{avg} = 1$ in the saturation regime. In all the calculations, we set $f_{rf} = 1$ GHz. For the single-frequency case, we set $E_{rf} = 3$ MV/m, and for the cases with two carrier frequencies, we set $E_{rf} = 3/\sqrt{2}$ MV/m.

macroparticle impacts the surface, we emit this macroparticle again by assigning a random initial energy $E_0 = \frac{1}{2}mv_0^2$ and angle ϕ according to the following distributions [4]:

$$f(E_0) = \frac{E_0}{E_{0m}^2} e^{-\frac{E_0}{E_{0m}}}, \quad (4a)$$

$$g(\phi) = \frac{1}{2} \sin \phi, \quad 0 < \phi < \pi, \quad (4b)$$

where E_{0m} is the peak of the distribution of emission energies, on the order of the work function, i.e., a few eV. [2,4,37,38]. We adjust the charge and mass of this macroparticle according to the secondary electron yield, δ , of this impact. Total surface charge and normal electric field values are also updated accordingly with its charge-to-mass ratio unchanged [31]. The charges and masses of all the other macroparticles in flight are unchanged by this impact. The initial rf phase of our simulation is assigned as $\theta = 0$, and then it is calculated self-consistently ($\theta_{i+1} = \theta_i + \omega\tau_{min}$) at the beginning of each iteration [cf. Eqs. (1)–(3)], where τ_{min} is the time interval between the i th and $(i+1)$ th impacts. Note that since the initial electric field E_{x0} (i.e., the initial number of primary electrons) is assumed to be relatively large ($E_{x0} \sim E_{rf}/30$), the specific choice of the initial rf phase θ does not affect the result of the temporal study. The ac saturation state can be obtained by starting the simulation with any value of θ . It is worthwhile to mention that, though space-charge effects are not accounted for in the multiparticle Monte Carlo simulation, previous results on multipactor dynamics are demonstrated to match well with those obtained from particle-in-cell simulations (cf. Fig. 2(a) of Ref. [31], Fig. 3(b) of Ref. [16], and Fig. 8(a) of Ref. [29]).

III. TIME-DEPENDENT FIELDS AND SECONDARY ELECTRON YIELD

With the addition of the second carrier mode, the overall rf electric field will become periodically modulated, which is expected to distort the electrons' trajectory, leading to modified multipactor dynamics [31]. Figure 2 shows the temporal profiles of the rf signal E_y (solid blue lines), secondary electron yield δ (dotted red lines), and normal electric field E_x (broken black lines) for two-frequency excitations with various γ , and with fixed $n = 2$, $\beta = 1$, and $f_{rf} = 1$ GHz. In Fig. 2(a), the single-frequency rf signal E_y with amplitude $E_{rf, single} = 3$ MV/m produces the secondary electron yield δ and the normal electric field E_x that oscillate at twice the rf frequency as shown previously by Kim and Verboncoeur [29]. Figures 2(b)–2(d) show the same plots for two-frequency rf signals. Individual carrier amplitudes of the two-frequency signals in Figs. 2(b)–2(d) are chosen as $E_{rf, dual} = E_{rf, rms, single} = 3/\sqrt{2}$ MV/m so that the average rf power of a two-frequency signal is equal to the average rf power of the single-frequency signal. Figures 2(e)–2(h) show the closed Lissajous curves for the field configurations of Figs. 2(a)–2(d) respectively, describing the temporal relationship between the fields normal (E_x) and parallel (E_y) to the surface. The shaded cyan region in the Lissajous curves indicates the parameter regime where the multipactor discharge grows. When both components of the electric field (E_x, E_y) are in this shaded regime, it is expected that the number of electrons N_s grows due to multipaction and the normal electric field E_x increases. Otherwise, the normal electric field E_x and hence the multipactor electron population N_s decrease.

TABLE I. Time spent by the electric fields in the growth and decay regions and the time-averaged normal electric field values for different rf field configurations obtained from the temporal investigation of Fig. 2.

RF field configuration	Percentage of time spent in growth (decay) regime during one rf period (1 ns) of the fundamental frequency		Time-averaged normal electric field E_x (MV m ⁻¹)
	In large loops	In small loops	
Single frequency	20% (80%)	0% (0%)	0.9
Two frequency	$n = 2, \beta = 1, \gamma = 0$	13% (54%)	0.756
	$n = 2, \beta = 1, \gamma = \pi/2$	8% (25%)	0.775
	$n = 2, \beta = 1, \gamma = \pi$	13% (54%)	0.75

Careful examination of the temporal profiles shows that there is a slight overshoot when crossing the boundaries: the growth continues for a short time after the curve exits the shaded cyan region, and likewise, decay continues for a short time after the curve enters the shaded cyan region. This is because when the electric fields (E_x, E_y) enter the growth regime from the decay regime, there are some particles approaching the end of their flight periods that have had small energy gain during their flights. These particles impact the surface with low impact energies, yielding $\delta < 1$. Therefore, decay continues for a short time until the particles born in the growth regime start impacting the surface and overwhelm the low energy impacts of the particles born earlier in the decay regime. Similarly, when the electric fields (E_x, E_y) enter the decay regime from the growth regime, growth continues for a short time until the particles born in the decay regime can overcome the high energy impacts of the particles born earlier in the growth regime.

We find in Fig. 2(b) that when $n = 2, \beta = 1$, and $\gamma = 0$ the temporal profiles of the secondary electron yield δ and normal electric field E_x oscillate at four times the rf frequency [31] and consequently there are two large loops and two small loops in the closed Lissajous curve of Fig. 2(f). In Fig. 2(c), the temporal profiles of δ and E_x oscillate at three times the rf frequency for $\gamma = \pi/2$. As a result, there are two relatively small loops and one relatively large loop in the closed Lissajous curve of Fig. 2(g), resulting in a periodic asymmetry of electric field conditions in the horizontal y direction. Figures 2(d) and 2(h) show the temporal profiles of E_y, δ, E_x , and the corresponding closed Lissajous curve, respectively, for $\gamma = \pi$. It is noteworthy that the rf fields (E_y) for $\gamma = 0$ and $\gamma = \pi$ are similar but acting in opposite directions. Therefore, the temporal profiles of δ and E_x in Fig. 2(d) have oscillation patterns similar to those of Fig. 2(b), as is the case for the Lissajous curves in Figs. 2(h) and 2(f).

By interpolating the values of E_y where the Lissajous curves cross the susceptibility boundaries and substituting these values in $E_y = E_{rf} \sin(\omega t + \theta) + \beta E_{rf} \sin[n(\omega t + \theta) + \gamma]$ for Figs. 2(e)–2(h), we can determine the corresponding values of time t and quantify the amount of time in a period spent by the electric fields in the growth regime (shaded cyan region of the susceptibility diagram) and in the decay regime (white region of the susceptibility diagram). We also compare the time-averaged normal electric fields due to surface charging, corresponding to the multipactor strengths in the system, for the single-

and two-frequency operations. The results are summarized in Table I.

Note that for the two-frequency cases, the time in the growth regime in the small loops are relatively long, where the growth rate is low, resulting in a relatively small multipactor electron population during this time interval. In contrast, the time spent in the growth regime of the large loops in these cases is much shorter than that of the single-frequency case. The time-averaged normal electric field in the two-frequency cases (< 0.78 MV/m), corresponding to the multipactor strength in the system, is reduced from that of the single-frequency case (~ 0.9 MV/m) for the same rf power.

Figure 3 shows temporal profiles of the rf signal E_y (solid blue lines), secondary electron yield δ (dotted red lines), and normal electric field E_x (broken black lines) for $n = 2$ and $\gamma = \pi/2$, when the relative strength β decreases from 1, 0.75, and 0.5 to 0.25. As β decreases from Figs. 3(a)–3(d), the oscillation in the temporal profiles of E_x and δ gradually transfers from three times the rf frequency to twice the rf frequency. The third loop in the Lissajous curve gradually disappears from Figs. 3(e)–3(h) and two loops remain, resembling the single-frequency case. This is consistent with the results of Iqbal *et al.* [23] where the effect of the second carrier mode on the multipactor susceptibility becomes less prominent as the relative strength of the second carrier mode decreases.

IV. TIME-AVERAGED MULTIPACTOR SUSCEPTIBILITY

To calculate the multipactor susceptibility diagram, we use the multiparticle MC model described in Sec. II, but keep the normal electric field E_x fixed at its input value throughout the simulation [3,5,23]. The average value of secondary electron yield over n_i impacts (or iterations) is calculated as $\bar{\delta} = (\delta_1 \delta_2 \cdots \delta_{n_i})^{1/n_i}$, where a large n_i is used in the calculation ($n_i \sim 80\,000$ impacts for $N = 200$ macroparticles here) to estimate the $\bar{\delta}$ over a time duration corresponding to an integer multiple of an rf period. This average value $\bar{\delta}$ represents either a growing ($\bar{\delta} > 1$) or decaying ($\bar{\delta} < 1$) trend in the number of electrons in the avalanche, which depends on the input parameters, $E_x, E_{rf}, \delta_{\max 0}, n, \beta$, and γ . The boundaries of the multipactor susceptibility are determined where $\bar{\delta} = 1$.

It is important to stress that, in this study, we use the electric field of the form $E_y = E_{rf} \sin(\omega t + \theta) + \beta E_{rf} \sin[n(\omega t + \theta) + \gamma]$, as shown in Fig. 1 and in Eq. (1), where the relative phase between the two carriers,

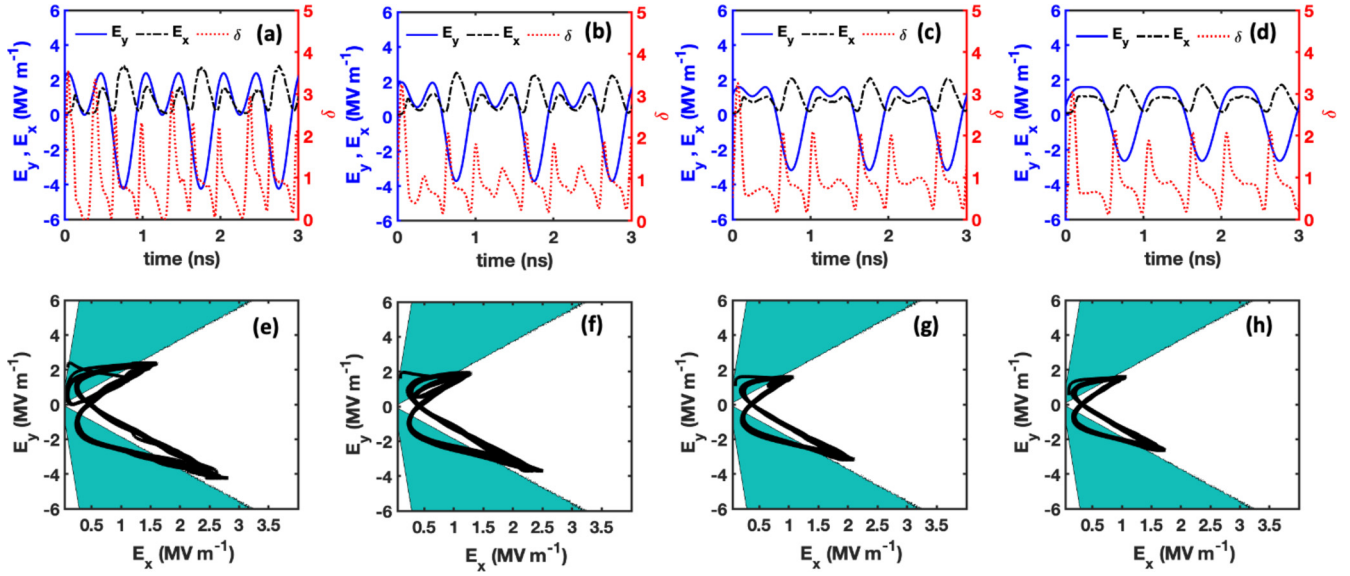


FIG. 3. Top row: Instantaneous rf electric field E_y (solid blue lines), normal electric field E_x (broken black lines), and secondary electron yield δ (dotted red lines), for two-frequency cases with frequency ratio $n = 2$, initial relative phase of the second carrier frequency, $\gamma = \pi/2$, and relative strength of the second carrier frequency, (a) $\beta = 1$, (b) $\beta = 0.75$, (c) $\beta = 0.5$, and (d) $\beta = 0.25$. Bottom row: (e–h) The corresponding plots of trajectories of the electric field $[E_x(t), E_y(t)]$ for (a–d), respectively. The shaded cyan region is the multipactor susceptibility region obtained by applying constant electric field, $E_{y,dc}$, parallel to the surface [29,31,39]. In (a)–(d), the average secondary electron yield $\delta_{\text{avg}} = 1$ in the saturation regime. In all the calculations, we set $f_{\text{rf}} = 1$ GHz and $E_{\text{rf}} = 3/\sqrt{2}$ MV/m.

$\Theta_{\text{relative}}(t) = (n - 1)(\omega t + \theta) + \gamma$, evolves self-consistently with time at each iteration. This is in contrast to Ref. [23], where the relative phase between the two carriers was kept constant as $\Theta_{\text{relative}} = \gamma$ at the beginning of each iteration.

Figure 4 shows the comparison of the two-frequency fields induced multipactor susceptibility diagrams with constant relative phase of the two carriers as in Ref. [23], and with evolving relative phase, for $n = 2$ and $\beta = 1$. For the cases

of constant relative phase in Figs. 4(a)–4(d), the slopes of both upper and lower susceptibility boundaries increase significantly, as γ increases from 0 to π [23]. However, for the cases of relative phase evolving with time in Figs. 4(e)–4(h), the slope of the lower susceptibility boundary decreases slightly as γ increases from 0 to $\pi/2$ and then increases again with $\gamma = \pi$, while the upper susceptibility boundary remains almost unaffected by the change of γ . While Ref. [23] con-

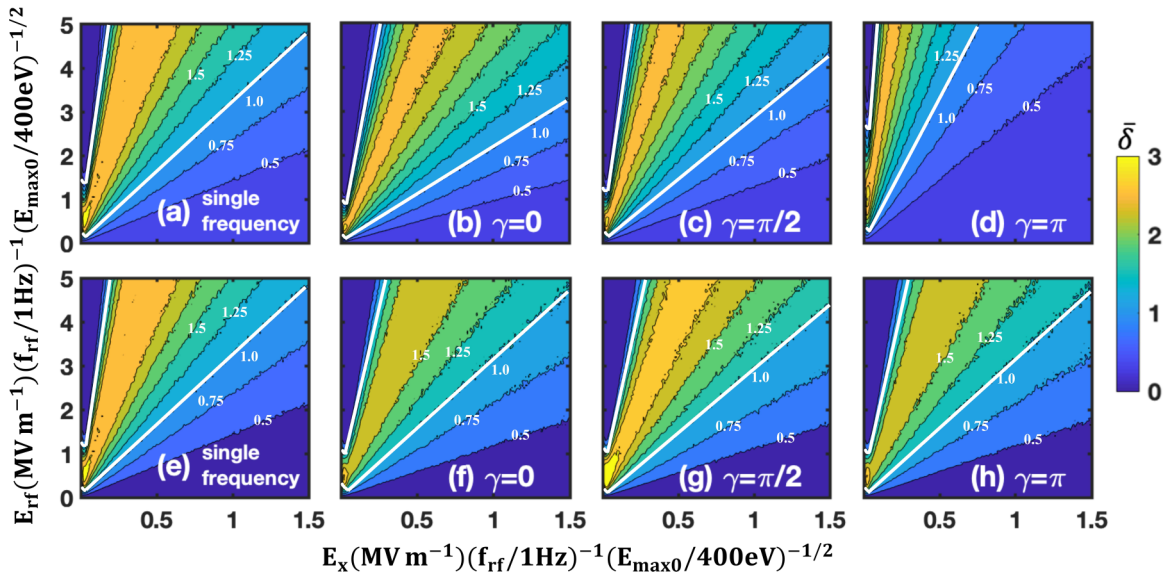


FIG. 4. Multipactor susceptibility with two carrier frequencies of the rf field from MC simulation for different γ in Eq. (1), for $\delta_{\text{max}0} = 3$, $E_{0m}/E_{\text{max}0} = 0.005$, relative frequency of the second carrier, $n = 2$, and relative strength of the second carrier, $\beta = 1$. Top row: the relative phase is kept fixed at the initial value over time [23]; bottom row: the relative phase evolves with time.

cludes that the presence of a second carrier mode can change the multipactor susceptibility boundaries, with the highest threshold achieved at $\gamma = \pi$, our present study shows that the effect of γ on the susceptibility boundaries is not prominent when the relative phase between the two carriers evolves over time.

Note that the assumption of constant relative phase of the second carrier in Iqbal *et al.* [23] is reasonable during the early stage of multipactor discharge if the frequency ratio of the two carriers, n , is very close to unity and therefore the evolution of relative phase is slow with time. When the frequency ratio n is not close to unity, the relative phase evolves quickly with time, which has to be self-consistently considered, as in Figs. 4(e)–4(h) from our multiparticle MC model.

The threshold rf and the corresponding normal electric fields (i.e., $E_{\text{rf,th}}$ and $E_{x,\text{th}}$, respectively) for multipactor discharge can be estimated at the lower susceptibility boundaries of the single- and two-frequency susceptibility diagrams of Figs. 4(e)–4(h) where $\bar{\delta} = 1$. For a given set of β , γ , and n , the values of the threshold normal electric fields should be equal to the time-averaged saturation levels of the electric fields obtained from the temporal analysis in the rf saturation state (described in Sec. III). The average rf power threshold per unit area (i.e., intensity) for multipactor discharge induced by two-frequency rf operation can be calculated as $P_{\text{rf,th}} = c\epsilon_0 E_{\text{rf,th}}^2 (1 + \beta^2)/2$.

For the single-frequency case, the saturation level of E_x estimated from the susceptibility diagram of Fig. 4(e) is about 0.9 MV/m with a given $E_{\text{rf,single}} = 3$ MV/m. For the two-frequency cases with $E_{\text{rf,dual}} = 3/\sqrt{2}$ MV/m for the same input power as of the single-frequency case, the saturation levels of E_x estimated from the susceptibility diagrams of Figs. 4(f)–4(h) are about 0.73, 0.76, and 0.73 MV/m, respectively. These values are in excellent agreement with the values obtained from our temporal investigation shown in Table I above.

V. MULTIPACTOR ELECTRON TRAJECTORIES AND PHASE SPACE

We have examined the multipacting particle trajectories for different rf field configurations when a second carrier mode is present in the rf field, as shown in Figs. 5(a) and 5(b). In our simulation, the vertical and horizontal excursions, controlled by the normal and parallel electric fields, respectively, of $N = 50$ macroparticles are monitored over time. The charge contained in the macroparticles is shown in the color scale bar on the right side of each plot. For charge neutrality, the total charge contained in the macroparticles is equal to the total surface charge N_s , which corresponds to the normal electric field E_x at $x = 0$. In both plots of Figs. 5(a) and 5(b), as the normal electric field (or total surface charge N_s) increases, the particles are drawn close to the surface and consequently their vertical excursions are small. During this period, their flight times are reduced, and they impact the surface with less energy. As a result, the secondary electron yield (SEY) drops [see Figs. 2(a) and 2(b)] and the normal electric field grows weaker. When the normal electric field is weak, the macroparticles containing less charge than before make farther excursions from the surface. Their flight times

increase, allowing them to gain more energy from the rf electric fields, which consequently increases the SEY of the impacts [Figs. 2(a) and 2(b)]. As a result, the normal electric field increases again and brings the trajectories of the particles closer to the surface. This process continues periodically, at twice the rf frequency for the single-frequency operation in Fig. 5(a), and at three times the fundamental rf frequency for the two-frequency operation with $\beta = 1$, $n = 2$, and $\gamma = \pi/2$ in Fig. 5(b).

The horizontal excursions of the particles depend on the rf electric field acting parallel to the surface. The macroparticles, containing negatively charged electrons, accelerate in the opposite direction of the rf electric field. For the single-frequency case, the rf field has periodic symmetry in the positive and negative y directions. Therefore, the horizontal excursion of the particles during the positive half cycle of the rf period is compensated during the negative half cycle of the rf period and the mean horizontal displacement of the particles is almost negligible over the complete rf period, as evident from Fig. 5(a). However, for the two-frequency case, the periodic symmetry of the rf field in the y direction is typically not present, as seen from Figs. 2(c) and 3(a)–3(d). During a fundamental rf period of 1 ns for $\beta = 1$, $n = 2$, and $\gamma = \pi/2$, the rf field acts in the $+y$ direction for roughly 0.67 ns and in the $-y$ direction for roughly 0.33 ns. Due to the periodic asymmetry of the rf field, a mean horizontal excursion of the negative charges in the $-y$ direction in one fundamental rf period is observed, as shown in Fig. 5(b).

The mean horizontal displacements with time for various two-frequency fields are summarized in Figs. 5(c) and 5(d). Figure 5(c) shows that for three cases: the single-frequency field (solid black line), i.e., $\beta = 0$, as well as for the two-frequency rf fields with $\beta = 1$, $n = 2$, and $\gamma = 0$ (dashed gray line) and π (dotted light gray line), the mean horizontal displacement of the macroparticles is almost negligible over the complete rf period. This is due to the periodic symmetry of the rf electric fields, as shown in Figs. 2(a), 2(b), and 2(d). For $0 < \gamma < \pi$, the periodic asymmetry of the rf field causes a mean horizontal displacement of the macroparticles in the $-y$ direction and the maximum horizontal displacement occurs for $\gamma = \pi/2$ [bottom curve in Fig. 5(c)]. On the other hand, for $\pi < \gamma < 2\pi$, the periodic asymmetry of the rf field causes a mean horizontal displacement of the macroparticles in the $+y$ direction and the maximum horizontal displacement occurs for $\gamma = 3\pi/2$ [top curve in Fig. 5(c)]. When the relative strength of the second carrier mode is lower, i.e., $\beta = 0.5$ in Fig. 5(d), the magnitudes of the mean horizontal displacement of the macroparticles decrease compared to those of $\beta = 1$. However, the directions of the mean horizontal displacements for $0 < \gamma < \pi$ and $\pi < \gamma < 2\pi$ remain the same for both $\beta = 1$ and $\beta = 0.5$. Therefore, we can summarize that the magnitude and the direction of the mean horizontal displacement of the macroparticles depend on the relative strength, β , and initial relative phase, γ , of the second harmonic carrier mode, respectively. This capability of migrating multipactor trajectories has been referred to as the steerability-to-zero criterion [25] and it can be of interest to rf system operators in applications such as cleaning a given location in a structure to reduce further susceptibility to multipactor, or for directing

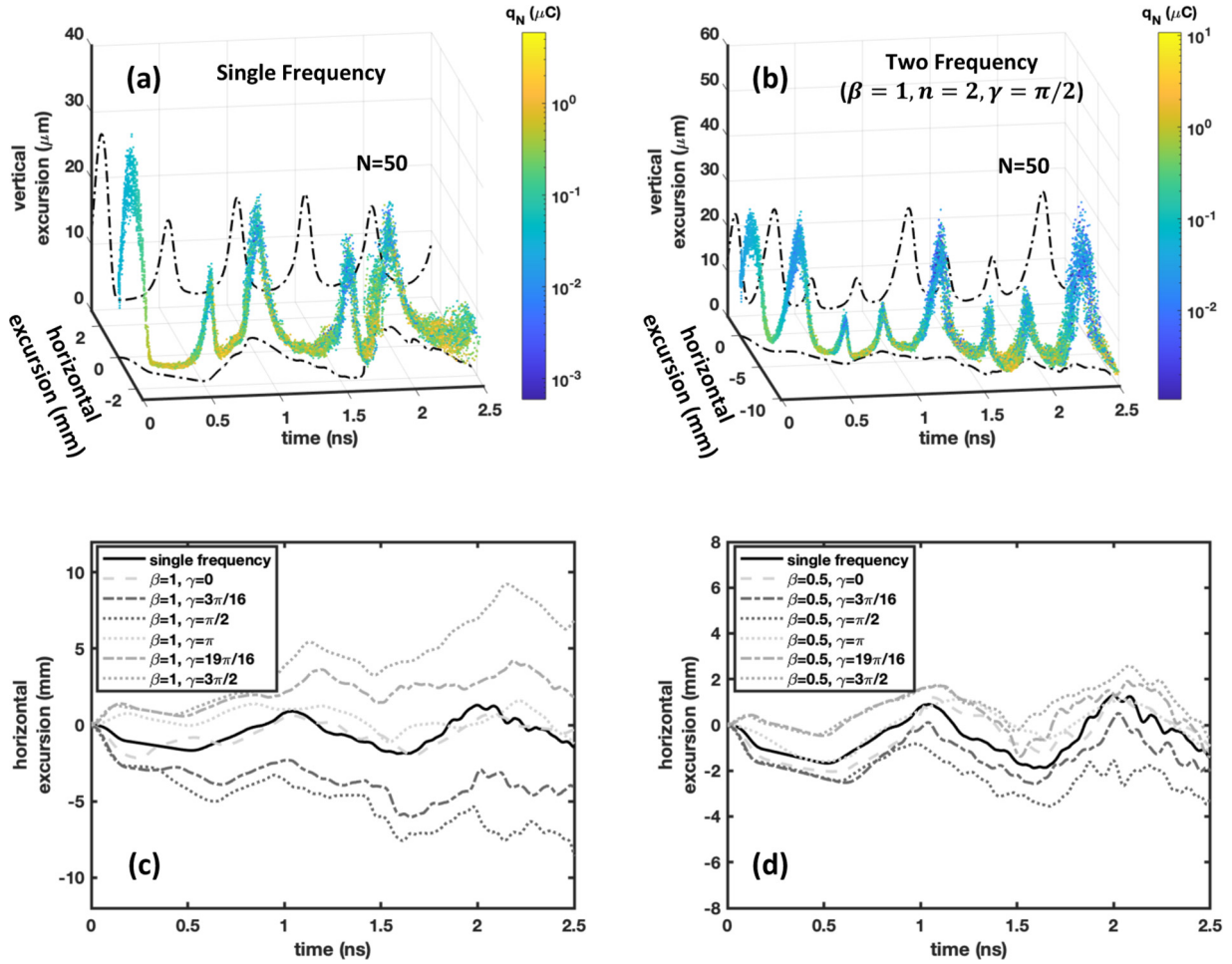


FIG. 5. Top row: Horizontal (along the dielectric surface) and vertical (normal to the surface) excursions of $N = 50$ multipacting macroparticles with respect to time, for (a) single-frequency rf electric field with $f_{\text{rf}} = 1$ GHz, and (b) two-frequency rf electric field with $f_{\text{rf}} = 1$ GHz, $\theta = 0$, $\beta = 1$, $n = 2$, $\gamma = \pi/2$. Charge contained in the macroparticles is shown in the color bar. Mean displacements of the macroparticles with respect to time are shown as projections on the horizontal and vertical planes. Bottom row: Comparison of the mean horizontal displacements for the single- and two-frequency rf electric fields with $f_{\text{rf}} = 1$ GHz, $\theta = 0$, $n = 2$, and $\gamma = 0, 3\pi/16, \pi/2, \pi, 19\pi/16$, and $3\pi/2$, for (c) $\beta = 1$ and (d) $\beta = 0.5$.

multipacting electrons to a specific desirable location in the geometry [25].

Figures 6 and 7 show the velocity-position phase space of $N = 50$ macroparticles during two rf periods in the vertical and horizontal directions respectively, for both single-frequency and two-frequency operation. In the $x - v_x$ phase space in Fig. 6, there is a periodic bunching and debunching of the macroparticles within an rf period. This happens because in our simulation, secondary macroparticles emitted from the $x = 0$ position are assigned random emission velocities in the $+x$ direction and the normal electric field E_x always acts in the $-x$ direction. When the normal field E_x is weak [e.g., $t = 0.5T_{\text{rf}}$, T_{rf} for single-frequency operation, cf. Fig. 2(a); and $t = 0.25T_{\text{rf}}$ for two-frequency operation, cf. Fig. 2(c)], the randomness of emission velocities results in a larger span of vertical positions of the macroparticles, and the vertical excursions of the macroparticles are large. However, when the normal field E_x is very strong [e.g., $t = 0.25T_{\text{rf}}$, $0.75T_{\text{rf}}$ for single-frequency operation, cf. Fig. 2(a); and $t = 0.75T_{\text{rf}}$ for two-frequency operation, cf. Fig. 2(c)],

it exerts more force and causes the macroparticles to stay closer to the surface, reducing the effect of the randomness of their emission velocities and resulting in a bunching effect in the $x - v_x$ phase space. The periodicity of bunching and debunching of the macroparticles in the phase space results from the periodic increase and decrease of the strength of the normal electric field. Note that including the space-charge shielding in the model would increase the distribution in vertical positions, since the most distant particles would see a weaker restoring field than the particles closer to the surface.

In contrast to Fig. 6, we observe in Fig. 7 a gradual debunching effect taking place in the horizontal velocity-position $y - v_y$ phase space. This is because the horizontal displacement is determined by the rf electric field that not only changes in strength but also changes in direction periodically. The emitted secondary macroparticles are assigned random emission angles uniformly distributed in the range of $[0, \pi]$. Therefore, the directions of the emission velocities of the macroparticles may be the same as or opposite to that of the

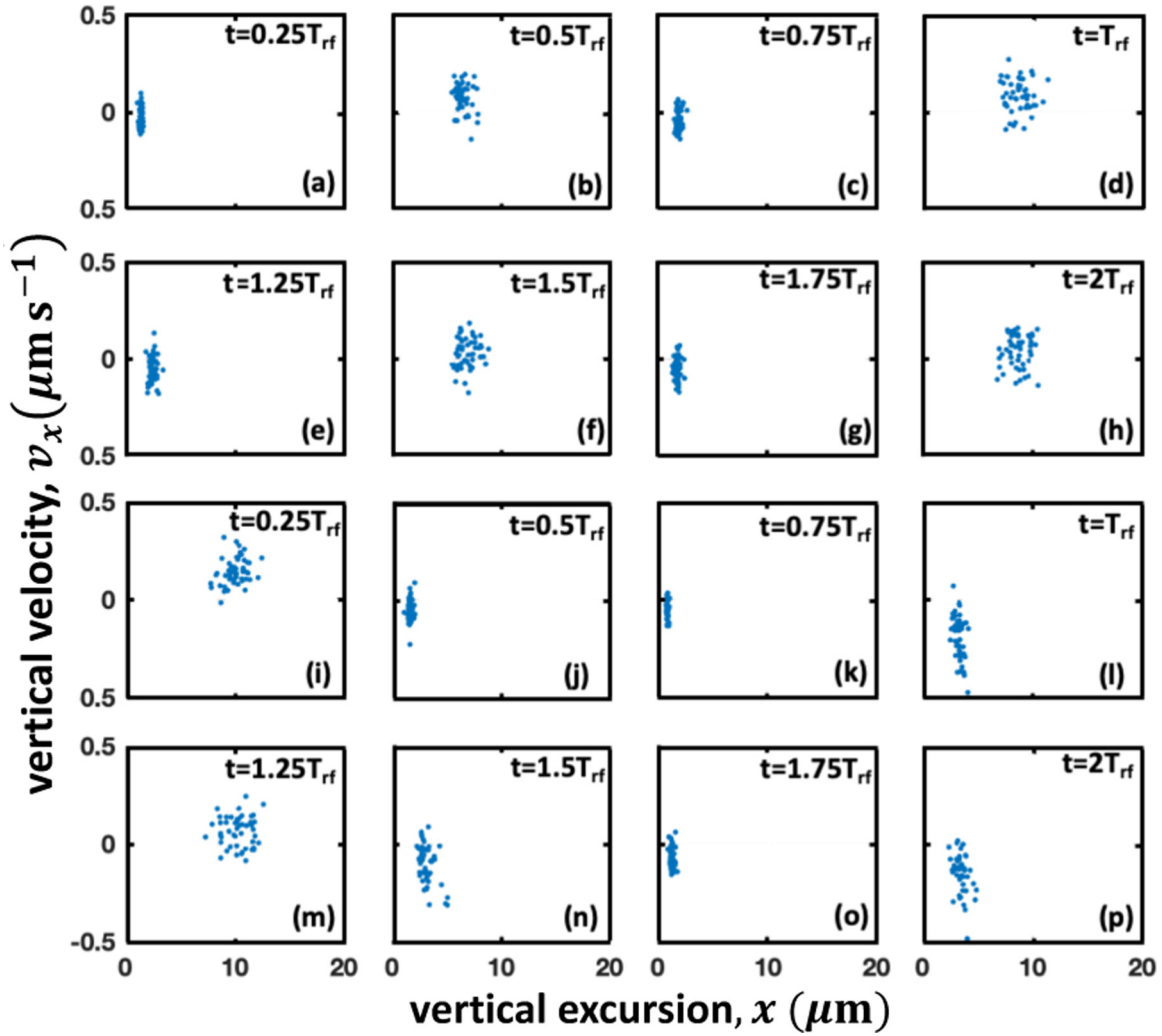


FIG. 6. Top two rows: v_x vs x for the single-frequency case at times (a) $t = 0.25T_{rf}$, (b) $t = 0.5T_{rf}$, (c) $t = 0.75T_{rf}$, (d) $t = T_{rf}$, (e) $t = 1.25T_{rf}$, (f) $t = 1.5T_{rf}$, (g) $t = 1.75T_{rf}$, and (h) $t = 2T_{rf}$, where $T_{rf} = 1$ ns is the rf period. Bottom two rows: (i–p) v_x vs x for the two-frequency case with $\beta = 1$, $n = 2$, and $\gamma = \pi/2$ at the same times as (a–h), respectively.

rf field, causing a dispersion in the $y - v_y$ phase space. This span increases with time as new generations of secondary macroparticles are emitted from different y locations and their emission velocities and emission angles add more randomness to the phase space.

Another important observation of Fig. 7 is the migration of multipactor trajectories for the dual-frequency operation. For the single-frequency case, the velocities of the macroparticles are in the $-y$ direction during the positive half cycle of the rf period [Figs. 7(a) and 7(b)], and in the $+y$ direction during the negative half cycle of the rf period [Figs. 7(c) and 7(d)]. The macroparticles do not have obvious net horizontal displacement due to this symmetry in the direction of velocities within a period. However, for the two-frequency case, the velocities of the macroparticles are in the $-y$ direction during most of the rf cycle [Figs. 7(i), 7(j), and 7(l)] and as a result, there is a net horizontal displacement of the particles in the $-y$ direction, which is consistent with Fig. 5(c).

VI. EFFECT OF FREQUENCY SEPARATION

Figure 8 shows the two-frequency susceptibility diagrams and temporal profiles of E_y , E_x , and δ for three cases with a noninteger frequency ratio. The first column shows the results for the case with $f_1 = 1$ GHz and $f_2 = 1.1$ GHz, the second column for the case with $f_1 = 1$ GHz and $f_2 = 1.25$ GHz, and the third column for the case with $f_1 = 1$ GHz and $f_2 = 1.5$ GHz. Figures 8(a)–8(c) have little difference, showing that multipactor susceptibility is relatively insensitive to the frequency separation, which is consistent with previous results in [23]. The reason for this insensitivity can be inferred from the temporal profiles of E_y and E_x in Figs. 8(d)–8(f). Due to the frequency separation the rf envelopes for the three cases are different. However, for the given $E_{rf} = 3$ MV/m, the time-averaged values of the resulting normal electric fields are almost the same, being 1.02 MV/m for Fig. 8(a), 1.03 MV/m for Fig. 8(b), and 1.03 MV/m for Fig. 8(c), respectively. From the susceptibility diagrams of Figs. 8(a)–8(c), the saturation

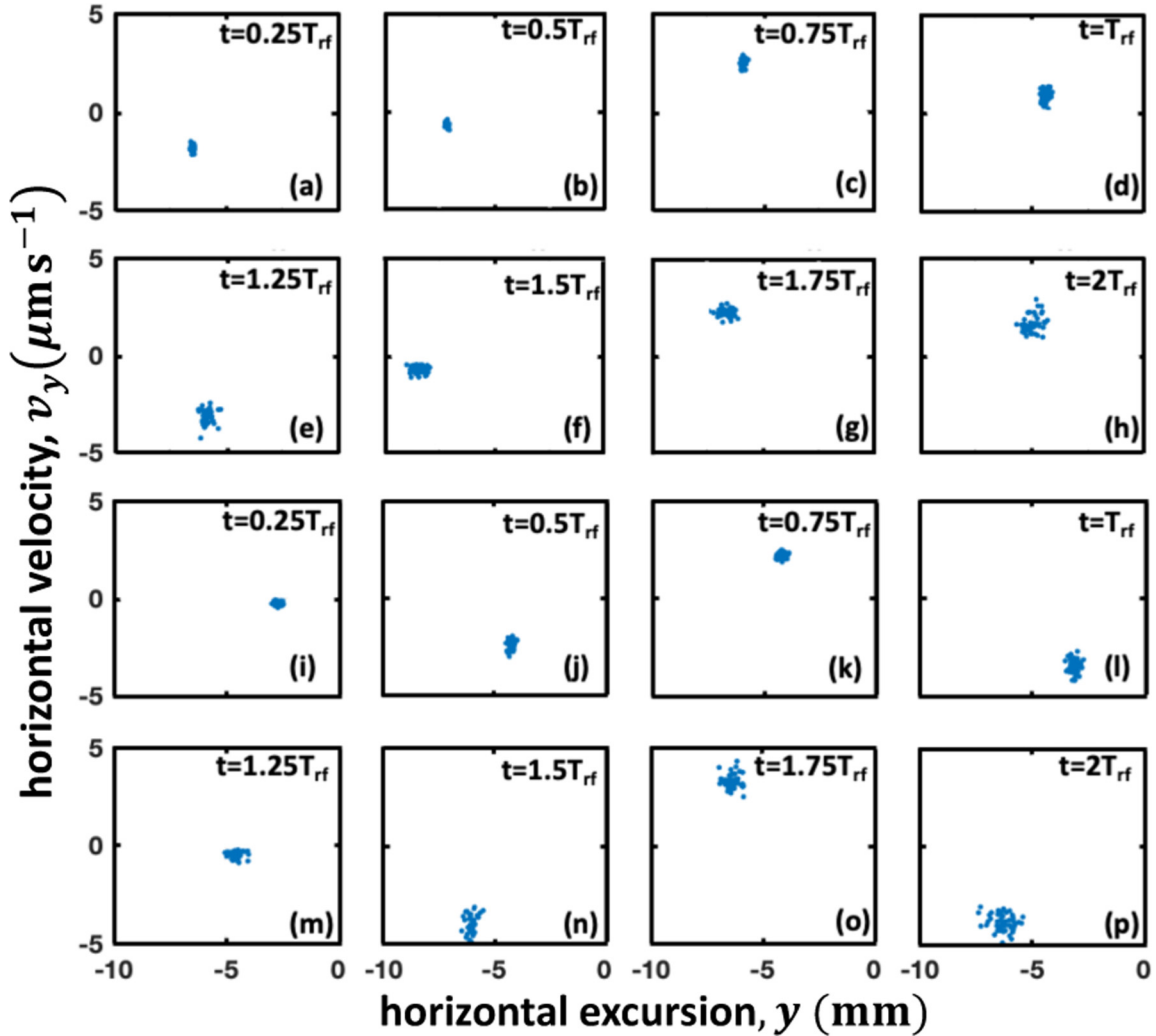


FIG. 7. Top two rows: v_y vs y for the single-frequency case at times (a) $t = 0.25T_{rf}$, (b) $t = 0.5T_{rf}$, (c) $t = 0.75T_{rf}$, (d) $t = T_{rf}$, (e) $t = 1.25T_{rf}$, (f) $t = 1.5T_{rf}$, (g) $t = 1.75T_{rf}$, and (h) $t = 2T_{rf}$, where $T_{rf} = 1$ ns is the rf period. Bottom two rows: (i–p) v_y vs y for the two-frequency case with $\beta = 1$, $n = 2$, and $\gamma = \pi/2$ at the same times as (a–h), respectively.

levels for the three cases are estimated to be ~ 1.0 , ~ 1.0 , and ~ 1.01 MV/m, respectively.

The periodic beating of the rf electric field E_y produces a beat wave in the temporal profiles of the normal surface charging electric field E_x . The beat frequency of such waves depends on the frequency separation, $\Delta f = f_2 - f_1$. The three representative cases with frequency separation of 100, 250, and 500 MHz have beat wave periods of 10, 4, and 2 ns, respectively. It is evident that multiple frequency components are present in the temporal profiles of the normal electric fields. These frequency components of the normal electric fields are analyzed through the frequency domain analysis of single-surface multipactor [16].

The insensitivity of multipactor susceptibility to the frequency separation of the two carrier modes is evident from Fig. 9. In Fig. 9(a), we observe that when the relative strength and phase of the second carrier mode is kept fixed at $\beta = 1$ and $\gamma = 0$ respectively, and the frequency ratio changes from $n = 1.05$ to $n = 1.5$, the two-frequency multipactor susceptibility boundaries remain almost unchanged. Figure 9(b) shows that for a fixed time-averaged saturation value of

the normal electric field E_x , the rf carrier amplitude at the lower susceptibility boundary in the ac saturation state, $E_{rf,sat}$, is insensitive to the frequency ratio n as well as to the relative phase of the second carrier mode γ . When $E_x = 0.5$ MV/m [dashed lines in Fig. 9(b)], for the frequency ratio, $1.05 \leq n \leq 1.50$, and relative phase of the second carrier mode, $0 \leq \gamma \leq \pi$, the rf carrier amplitude in ac saturation is found to be $E_{rf,sat} \sim 1.49$ MV/m. When E_x is increased to $E_x = 1.0$ MV/m [solid lines in Fig. 9(b)], the $E_{rf,sat}$ increases to $E_{rf,sat} \sim 2.98$ MV/m, remaining insensitive to both n and γ . These results have been spot checked against one-dimensional particle-in-cell (PIC) simulations.

VII. CONCLUDING REMARKS

This work presents a detailed investigation of the time-dependent physics of multipactor breakdown in single dielectric surfaces exposed to a transverse rf field with two carrier frequencies. The study was carried out using a multiparticle Monte Carlo simulation model in one dimension with adaptive time steps. The effects of the relative strength

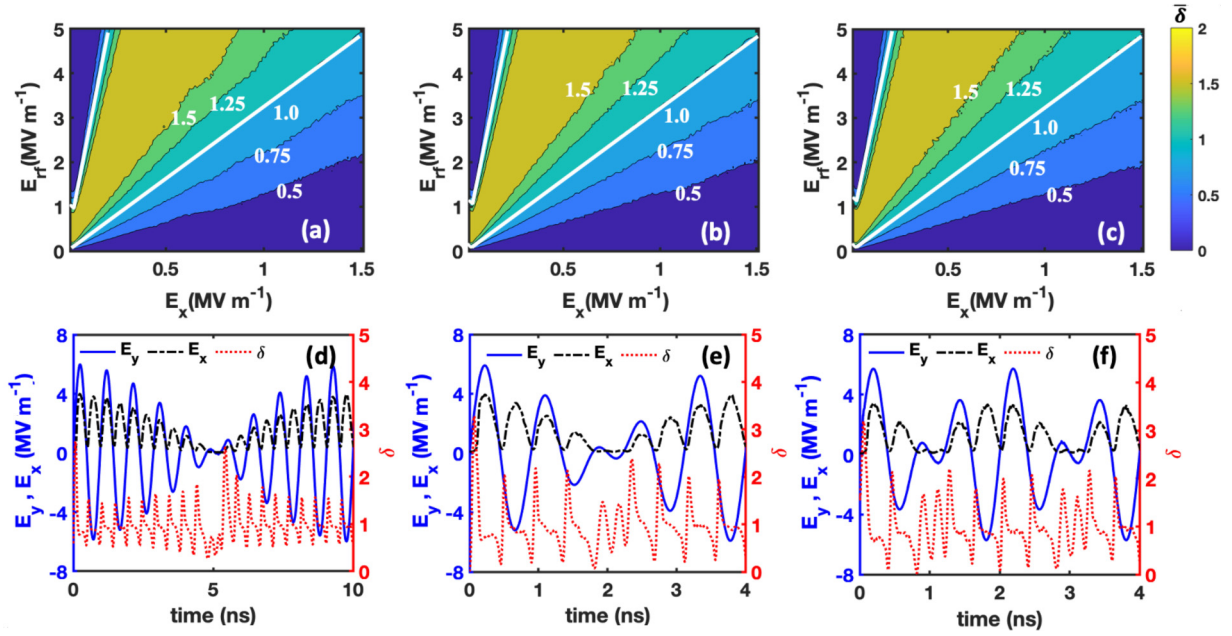


FIG. 8. Top row: Multipactor susceptibility diagrams for two-frequency rf fields with frequencies (a) $f_1 = 1$ GHz and $f_2 = 1.1$ GHz, (b) $f_1 = 1$ GHz and $f_2 = 1.25$ GHz, and (c) $f_1 = 1$ GHz and $f_2 = 1.5$ Hz. Bottom row: (d–f) The instantaneous rf electric field E_y (solid blue lines), normal electric field E_x (broken black lines), and secondary electron yield δ (dotted red lines) for rf field configurations of plots (a–c), respectively. In (d–f), the average secondary electron yield $\delta_{\text{avg}} = 1$ in the saturation regime. In all the calculations, we set, $\gamma = 0$, and $\beta = 1$.

β , relative phase γ , and the frequency separation of the two carrier frequencies on the temporal profiles of normal electric field E_x , corresponding to the multipactor strength, and the secondary electron yield δ are examined. It is found that when the relative phase evolves with time, the dependence of the two-frequency multipactor susceptibility boundaries on the initial relative phase γ is not as prominent as shown

in Ref. [23]. We have obtained closed Lissajous curves that describe the temporal relationship between the rf electric field and the normal electric field. The amount of time in a period spent by the fields in the multipactor growth regime and decay regime have been estimated for different two-frequency rf field configurations. Saturation levels of the normal electric field have been calculated from the time-dependent study and

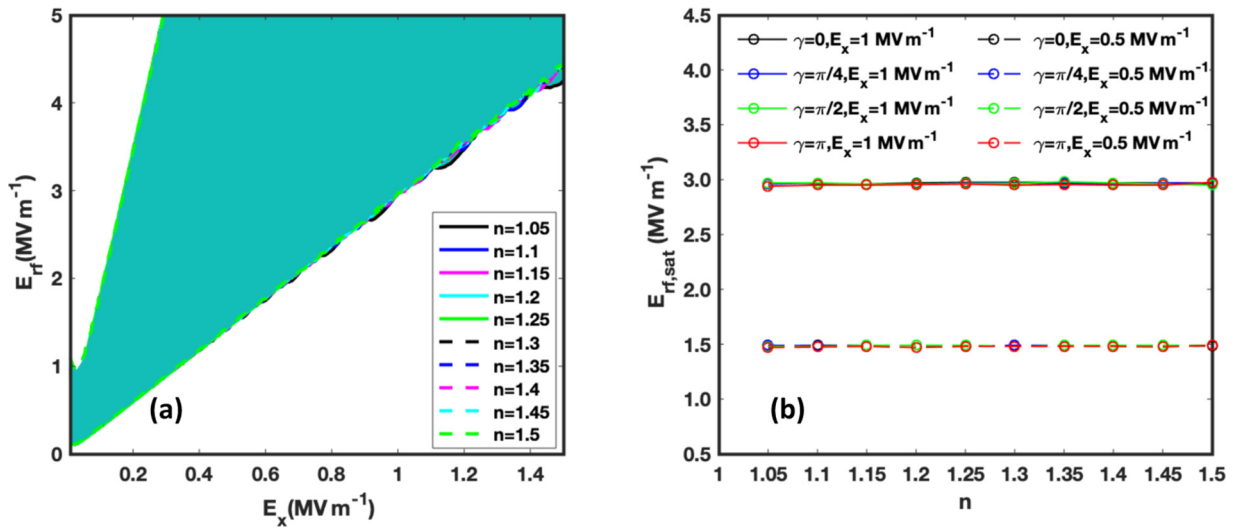


FIG. 9. (a) Multipactor susceptibility diagrams for two-frequency rf fields with $\beta = 1$, $\gamma = 0$, and frequency ratio $1.05 \leq n \leq 1.5$. The shaded cyan region shows the parameter regime where the multipactor discharge develops. The upper and lower susceptibility boundaries for different frequency ratio n are largely overlaid with one another. (b) Rf carrier amplitude at the lower susceptibility boundary in ac saturation state, $E_{\text{rf,sat}}$, for two-frequency rf operation with $\beta = 1$, $\gamma = 0, \pi/4, \pi/2$, and π for time-averaged saturation values of the normal electric field $E_x = 0.5$ MV/m (dashed lines) and 1.0 MV/m (solid lines). For a fixed value of E_x (0.5 or 1 MV/m), the E_{rf} vs n plots corresponding to different values of γ are overlaid with one another.

the susceptibility diagrams. It is found that the two-frequency operation can reduce multipactor strength while carrying the same total power as that of the single-frequency operation. As the relative strength of the second carrier mode decreases, its effect on multipactor discharge becomes less prominent. Multipactor susceptibility is insensitive to the frequency ratio (or frequency separation) of the two carrier modes. Beat waves have been observed in the temporal profiles of the normal electric field with a noninteger frequency ratio. It is demonstrated that migration of multipactor trajectories can be achieved by adding the second frequency carrier, which may be proposed as an effective method for multipactor mitigation. Our study here mainly focuses on two-frequency rf operation with the second harmonic of the fundamental carrier mode. This may be of practical importance because in different rf devices such as traveling wave tubes (TWTs), a strong second harmonic component of the input rf frequency is often generated [40,41] and the analysis of the multipactor discharge in such practical applications requires a close examination of the

effects of the second harmonic content of the fundamental rf frequency.

Further studies may include temporal investigation of nonsinusoidal wave shapes, multicarrier (more than two frequencies) operation, nontransverse rf modes, and the connection of single-surface and two-surface multipactor. Multipactor discharge for two- or multifrequency rf operation in the presence of background gases [5] or in dielectric loaded geometries [42,43] can also be of interest.

ACKNOWLEDGMENTS

The work was supported by the Air Force Office of Scientific Research (AFOSR) MURI Grant No. FA9550-18-1-0062, and an MSU Foundation Strategic Partnership Grant. A.I. also gratefully acknowledges the support through the Michigan Institute for Plasma Science and Engineering (MIPSE) Graduate Fellowship.

-
- [1] P. T. Farnsworth, *J. Franklin Inst.* **218**, 411 (1934).
 [2] J. R. M. Vaughan, *IEEE Trans. Electron Devices* **35**, 1172 (1988).
 [3] R. A. Kishek and Y. Y. Lau, *Phys. Rev. Lett.* **80**, 193 (1998).
 [4] R. A. Kishek, Y. Y. Lau, L. K. Ang, A. Valfells, and R. M. Gilgenbach, *Phys. Plasmas* **5**, 2120 (1998).
 [5] P. Zhang, Y. Y. Lau, M. Franzi, and R. M. Gilgenbach, *Phys. Plasmas* **18**, 053508 (2011).
 [6] A. J. Hatch and H. B. Williams, *J. Appl. Phys.* **25**, 417 (1954).
 [7] A. J. Hatch and H. B. Williams, *Phys. Rev.* **112**, 681 (1958).
 [8] D. H. Preist and R. C. Talcott, *IRE Trans. Electron Devices* **8**, 243 (1961).
 [9] J. R. M. Vaughan, *IRE Trans. Electron Devices* **8**, 302 (1961).
 [10] S. Yamaguchi, S. Michizono, and S. Anami, *IEEE Trans. Nucl. Sci.* **39**, 278 (1992).
 [11] D.-Q. Wen, P. Zhang, Y. Fu, J. Krek, and J. P. Verboncoeur, *Phys. Plasmas* **26**, 123509 (2019).
 [12] N. Rozario, H. F. Lenzing, K. F. Reardon, M. S. Zarro, and C. G. Baran, *IEEE Trans. Microwave Theory Tech.* **42**, 558 (1994).
 [13] Special sessions on Multipactor, I and II, IEEE ICOPS, Denver, CO, June, 2018.
 [14] P. Y. Wong, Y. Y. Lau, P. Zhang, N. Jordan, R. M. Gilgenbach, and J. Verboncoeur, *Phys. Plasmas* **26**, 112114 (2019).
 [15] V. E. Semenov, E. I. Rakova, N. A. Zharova, J. Rasch, D. Anderson, and J. Puech, *J. Phys. D: Appl. Phys.* **47**, 055206 (2014).
 [16] A. Iqbal, P. Y. Wong, J. P. Verboncoeur, and P. Zhang, *IEEE Trans. Plasma Sci.* **48**, 1950 (2020).
 [17] P. Y. Wong, P. Zhang, and J. P. Verboncoeur, *IEEE Trans. Plasma Sci.* **48**, 1959 (2020).
 [18] S. Anza, C. Vicente, B. Gimeno, V. E. Boria, and J. Armendáriz, *Phys. Plasmas* **14**, 082112 (2007).
 [19] S. Anza, C. Vicente, J. Gil, V. E. Boria, B. Gimeno, and D. Raboso, *Phys. Plasmas* **17**, 062110 (2010).
 [20] S. Anza, M. Mattes, C. Vicente, J. Gil, D. Raboso, V. E. Boria, and B. Gimeno, *Phys. Plasmas* **18**, 032105 (2011).
 [21] S. Anza, C. Vicente, J. Gil, M. Mattes, D. Wolk, U. Wochner, V. E. Boria, B. Gimeno, and D. Raboso, *IEEE Trans. Microwave Theory Tech.* **60**, 2093 (2012).
 [22] V. Semenov, A. Kryazhev, D. Anderson, and M. Lisak, *Phys. Plasmas* **8**, 5034 (2001).
 [23] A. Iqbal, J. Verboncoeur, and P. Zhang, *Phys. Plasmas* **25**, 043501 (2018).
 [24] F. Piro and Y. Brand, in *Proceedings of 8th European Conference on Antennas and Propagation (EuCAP), The Hague, Netherlands* (IEEE, Piscataway, NJ, 2014), pp. 1643–1646.
 [25] S. A. Rice and J. P. Verboncoeur, *IEEE Trans. Plasma Sci.* **45**, 1739 (2017).
 [26] M. Siddiqi and R. A. Kishek, *Phys. Plasmas* **26**, 113111 (2019).
 [27] A. A. Hubble, M. S. Feldman, P. T. Partridge, and R. Spektor, *Phys. Plasmas* **26**, 053502 (2019).
 [28] D.-Q. Wen, A. Iqbal, P. Zhang, and J. P. Verboncoeur, *Phys. Plasmas* **26**, 093503 (2019).
 [29] H. C. Kim and J. P. Verboncoeur, *Phys. Plasmas* **12**, 123504 (2005).
 [30] H. C. Kim and J. P. Verboncoeur, *Phys. Plasmas* **13**, 123506 (2006).
 [31] A. Iqbal, J. Verboncoeur, and P. Zhang, *Phys. Plasmas* **26**, 024503 (2019).
 [32] A. Valfells, L. K. Ang, Y. Y. Lau, and R. M. Gilgenbach, *Phys. Plasmas* **7**, 750 (2000).
 [33] C. Chang, G. Liu, C. Tang, C. Chen, S. Qiu, J. Fang, and Q. Hou, *Phys. Plasmas* **15**, 093508 (2008).
 [34] A. Neuber, J. Dickens, D. Hemmert, H. Krompholz, L. L. Hatfield, and M. Kristiansen, *IEEE Trans. Plasma Sci.* **26**, 296 (1998).
 [35] J. R. M. Vaughan, *IEEE Trans. Electron Devices* **36**, 1963 (1989).
 [36] R. M. Vaughan, *IEEE Trans. Electron Devices* **40**, 830 (1993).
 [37] A. Iqbal, J. Ludwick, S. Fairchild, M. Cahay, D. Gortat, M. Sparkes, W. O'Neill, T. C. Back, and P. Zhang, *J. Vac. Sci. Technol. B* **38**, 013801 (2020).

- [38] J. Ludwick, A. Iqbal, D. Gortat, J. D. Cook, M. Cahay, P. Zhang, T. C. Back, S. Fairchild, M. Sparkes, and W. O'Neill, *J. Vac. Sci. Technol. B* **38**, 054001 (2020).
- [39] A. Iqbal, J. Verboncoeur, P. Wong, and P. Zhang, in *Proceedings of 2019 International Vacuum Electronics Conference (IVEC)* (IEEE, Piscataway, NJ, 2019), pp. 1–2.
- [40] C. F. Dong, P. Zhang, D. Chernin, Y. Y. Lau, B. W. Hoff, D. H. Simon, P. Wong, G. B. Greening, and R. M. Gilgenbach, *IEEE Trans. Electron Devices* **62**, 4285 (2015).
- [41] P. Y. Wong, Y. Y. Lau, D. Chernin, B. W. Hoff, and R. M. Gilgenbach, *IEEE Trans. Electron Devices* **65**, 710 (2018).
- [42] A. Berenguer, Á. Coves, F. Mesa, E. Bronchalo, and B. Gimeno, *IEEE Trans. Plasma Sci.* **47**, 259 (2019).
- [43] A. Berenguer, Á. Coves, B. Gimeno, E. Bronchalo, and V. E. Boria, *IEEE Microwave Wireless Compon. Lett.* **29**, 595 (2019).